Design, fabrication, and tuning studies of the low beta high-gradient S-band traveling wave cryogenic copper cavity at the Institute of Modern Physics

Peng Yu,[1,2] Min Yang,[1] Quantang Zhao,[1,2,*] Xiaoxiao Yuan,[1] Chihao Ni,[1,2] Lejian Zhang,[1,2] Jiao Xu,[1,2] Yao Yang,[1,2] Zimin Zhang,[1,2] Liangting Sun,[1,2] and Hongwei Zhao[1,2]

[1]*Institute of Modern Physics, Chinese Academy of Sciences, Lanzhou, 730000, China*
[2]*College of Nuclear Sciences, University of Chinese Academy of Sciences, Beijing 100049, China*

(Received 11 November 2025; accepted 21 May 2026; published 23 June 2026)

The high-frequency, high-gradient, low-β accelerator structure is a key technology enabling compact ion linacs for hadron therapy, garnering significant interest in cancer treatment research. Currently, multiple institutions globally are advancing this technology. However, the achievable accelerating gradient remains limited to approximately 50 MV/m due to radio-frequency (rf) breakdown (BD) limitations. To enable higher accelerating gradients, researchers at the Institute of Modern Physics, Chinese Academy of Sciences, have proposed and designed a low-β high-gradient cryogenic copper cavity targeting a theoretical accelerating gradient of 60 MV/m with a specified breakdown rate (BDR $\leq 10^{-6}$ bpp/m). This paper details the design, fabrication, and tuning methodology of a $\beta = 0.3$ cryogenic traveling-wave high-gradient accelerating structure. Cell tests were performed to verify the cryogenic performance of the cavity. Upon cooling from room temperature to 77 K, the cavity's quality factor (Q) increased by a factor of 2.9, while its resonant frequency shifted upward by 9.85 MHz. Subsequently, a 15-cell cryogenic traveling-wave structure was fabricated and tuned to meet stringent design specifications. The conduction cooling methodology was experimentally validated, achieving a stable cavity temperature of 77 ± 0.3 K within 5 h. This work establishes a framework for tuning cryogenic traveling-wave copper cavities and implementing conduction cooling in high-gradient systems.

DOI: 10.1103/ndky-79h9

I. INTRODUCTION

Hadron therapy represents a crucial technology in cancer treatment, leveraging the Bragg peak to concentrate ionizing radiation precisely within tumors while minimizing damage to surrounding healthy tissue [1]. As of 2026, over 150 hadron therapy facilities operate globally, predominantly employing synchrotrons or cyclotrons that deliver protons at 70–230 MeV and carbon ions at 100–430 MeV/u [2]. However, these conventional accelerator systems exhibit several limitations, including high construction costs, large physical footprints, and limited ability to rapidly and automatically adjust beam energy during treatment [3].

To overcome these limitations, a compact high-energy proton linac for hadron therapy was first proposed in 1991 [4]. Over the past three decades, multiple institutions globally have advanced linac-based hadron therapy systems [5–9]. Notably, the Linac for Image-Guided Hadron Therapy, developed by Application of Detectors and Accelerators to Medicine, remains the sole operational high-gradient proton therapy system [9]. Modern designs feature an improved layout: a radio-frequency quadrupole (RFQ) accelerating ions to 10 MeV/u, an interdigital H-mode drift-tube linac (IH-DTL) reaching 70 MeV/u, a side-coupled drift-tube linac (SCDTL) covering 70–100 MeV/u, and a final high-frequency section boosting the beam to therapeutic energy [10].

In addition to layout improvements, various high-gradient linac options are available, which can be categorized into two distinct types: standing-wave and traveling-wave structures. Standing-wave configurations include the coupled-cell linac [11] and the single-periodic magnetically coupled standing-wave accelerating structure (SPMCS) [12]. These structures require a longer electromagnetic filling times than traveling-wave designs to reach nominal accelerating gradients, thereby limiting achievable gradients [13,14]. For instance, backward traveling-wave (BTW) cavities can achieve gradients up to 50 MV/m. However, in low-β sections ($\beta < 0.38$), the short acceleration gap limits performance. Consequently, the first negative-harmonic structure (NHS) featuring an elongated gap was implemented in the low-β ($\beta = 0.3$) section of the

*Contact author: zhaoquantang@impcas.ac.cn

Published by the American Physical Society under the terms of the Creative Commons Attribution 4.0 International license. Further distribution of this work must maintain attribution to the author(s) and the published article's title, journal citation, and DOI.

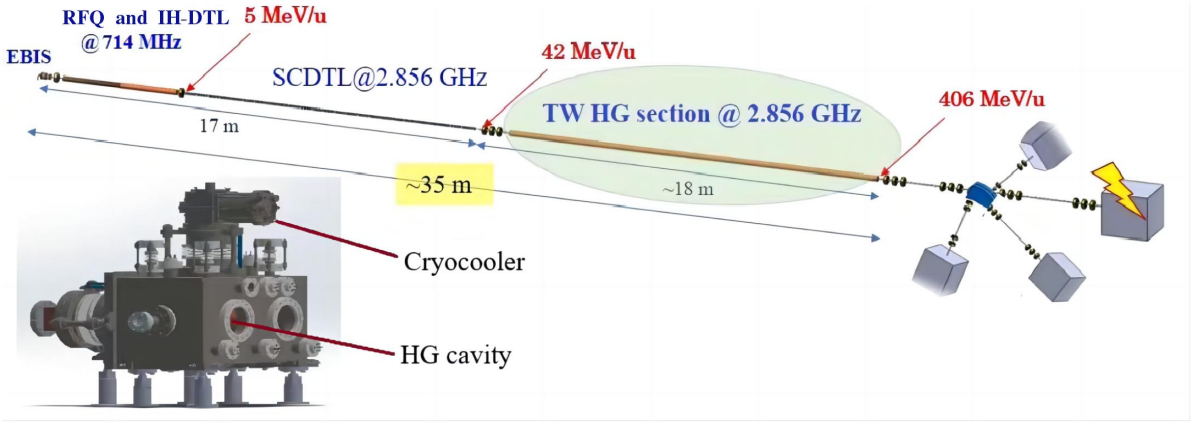


FIG. 1. Layout of an ultracompact cryogenic traveling-wave linac for carbon-ion therapy.

Advanced Compact Carbon Ion Linac [7], achieving a gradient of 50 MV/m [15].

The accelerating gradient in room-temperature S-band high-gradient cavities is primarily limited by radio-frequency (rf breakdown (BD), with the breakdown rate (BDR) increasing sharply at higher gradients [16]. Consequently, cryogenic copper cavities suppress the BDR by leveraging copper's reduced surface resistivity and enhanced mechanical hardness at cryogenic temperatures [17,18], enhancing thermal stability and reducing operating power consumption.

Several high-gradient linacs operate at cryogenic temperatures [19–21], but these are standing-wave cavities designed for electron acceleration. To achieve a more compact system for hadron therapy, we propose a cryogenic traveling-wave structure [22], with the overall layout shown in Fig. 1. Clarification of the Four Stages:

1. RFQ section (Room Temperature): Initial acceleration of hadrons to 2.3 MeV/u at 714 MHz.
2. IH-DTL section, (Room Temperature): Energy boosting to 5 MHz/u at 714 MHz.
3. SCDTL section, (Room Temperature): Energy boosting to 42 MeV/u at 2856 MHz.
4. High gradient section (77 K): 32 cryogenic traveling-wave cavities at 2856 MHz to achieve targeted energy levels.
   (a) NHS cavities (low-β section, $0.3 < \beta < 0.38$) with a target electric field gradient of 60 MV/m.
   (b) BTW cavities in the high-β section ($\beta \geqslant 0.38$), achieving an electric field gradient of 70 MV/m.

For low-β structures, the cell length is shorter, resulting in higher electric field intensity and a higher probability of breakdown. To mitigate this, a longer NHS structure is employed, which helps reduce the electric field strength and thereby lowers the risk of breakdown. For high-β structures, the cavity cell length is larger, leading to a reduced probability of breakdown. In the case of $\beta = 0.42$ BTW structure and $\beta = 0.3$ NHS structure having the same cell length [7], the optimization results in Fig. 2 show that the effective shunt impedances (ZTT) value of the NHS structure is lower than that of the BTW structure. Therefore, when β exceeds 0.38, the BTW structure is preferred as it allows for lower input power while maintaining performance, resulting in a more compact overall design.

The adopted layout requires 32 fewer cavities than the carbon booster for therapy in oncology (CABOTO) carbon-ion therapy design [13] in the high-gradient section, significantly reducing instabilities caused by cumulative alignment errors across multiple tanks.

In conventional external beam radiotherapy, the standard fractionation dose is typically maintained at 1.8–2.0 Gy per fraction [23]. This regimen, validated through decades of clinical practice, has proven effective for radical treatment of most solid tumors. However, with advancing understanding of tumor radiobiology and continuous technological innovations in radiotherapy, hypofractionated radiotherapy regimens have gained widespread clinical adoption across both curative and palliative settings for various malignancies [24,25]. This paradigm shift is driven by their distinct advantages, including enhanced treatment

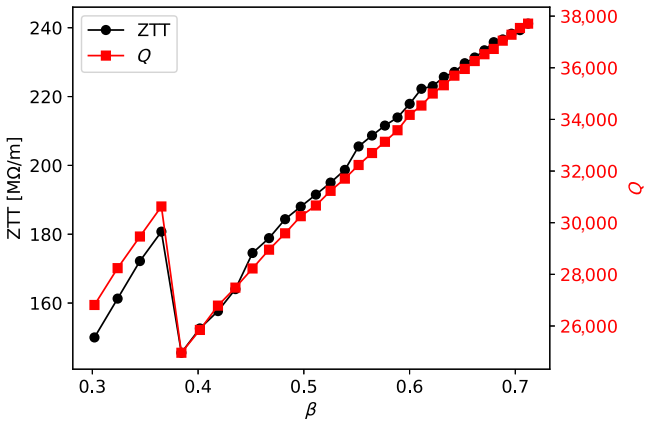


FIG. 2. Quality factors (Q) and effective shunt impedances (ZTT) for cryogenic high-gradient cavities.

convenience, improved cost-effectiveness, and rapid symptom palliation. Therefore, the system delivers a clinically validated dose of 2.6 Gy per fraction within 100 s, enabling conventional tumor therapy [26], supporting: (i) carbon-ion therapy at 2.2×10^8 particles/s (ii) helium-ion therapy at 6.5×10^8 particles/s.

During operation, rf pulse duration reaches 2500 ns with a repetition rate tunable between 50–120 Hz. Consequently, the following sections detail the design, fabrication, and tuning of a $\beta = 0.3$ cryogenic copper cavity.

II. LOW β CRYOGENIC S-BAND CAVITY RF DESIGN

A cryogenic NHS structure operating at 2856 MHz was designed to achieve an accelerating gradient exceeding 60 MV/m. The cavity comprises 13 regular cells and 2 coupling cells, optimized for carbon ions at $\beta = 0.3$. All electromagnetic simulations were performed using cst Studio Suite [27].

A. Limitations

The design of high-gradient cavities is constrained by the risk of rf breakdown, which is typically initiated by extremely high local surface electric or magnetic fields. Consequently, cavity design requires careful control of the peak surface electric field (E_{pk}) and peak surface magnetic field (H_{pk}). An enhanced surface electric field can induce high field emission currents, leading to localized melting of emission sites and triggering breakdown [28]. The empirical relationship between BDR and peak surface electric field is summarized by the scaling law [29]:

$$\frac{E_{pk}^{30} t_p^6}{\mathrm{BDR}} = \text{const}, \tag{1}$$

where t_p is the rf pulse width. For equivalent accelerating gradients, BDR decreases by 2 orders of magnitude when the operating temperature is reduced from 300 to 70 K in X-band structures [30]. For medical accelerators, the BDR requirement is determined by the design parameters and the specific needs of the end-user. In the initial design of CABOTO, a repetition rate of 400 Hz and a treatment duration of 5 min were proposed. To ensure that the expected number of breakdowns during the entire treatment remains below 1, a BDR requirement of 1×10^{-6} bpp/m was established [31]. For our proposed design, the repetition rate and treatment duration are lower, resulting in less stringent BDR requirements. Nevertheless, a BDR level of 1×10^{-6} bpp/m is adopted in order to extend the time interval between two consecutive BDR events. A room-temperature S-band BTW cavity achieves a peak surface field of 220 MV/m at 2500 ns pulse width [13]. Using the scaling law, the corresponding peak surface field for a cryogenic (77 K) S-band cavity at the same pulse width is predicted to be 255 MV/m. This prediction has been experimentally validated in cryogenic rf breakdown studies [32].

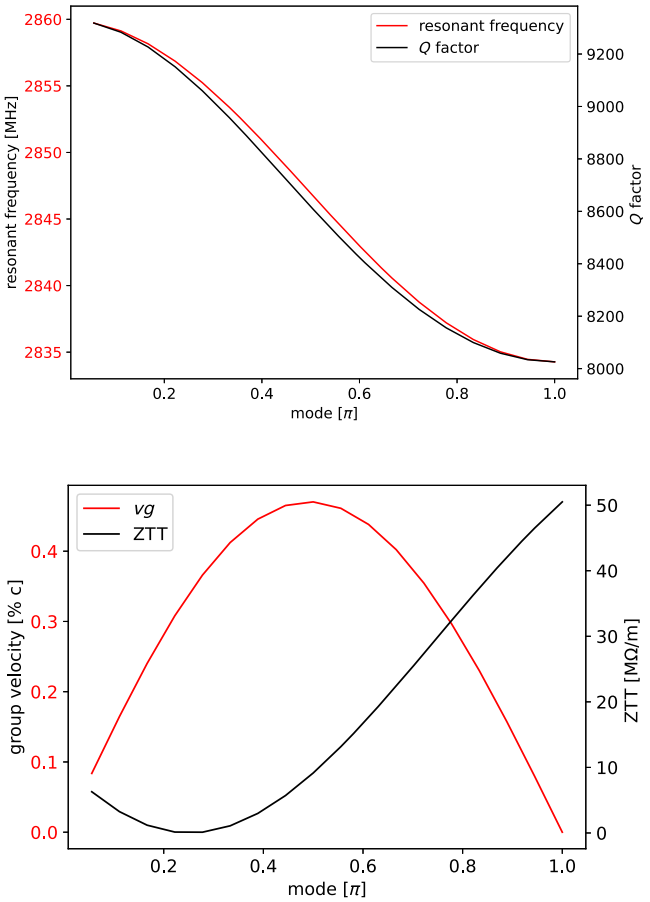


FIG. 3. Top: frequency (red), Q (black); bottom: group velocity (red), shunt impedance (black) versus operating mode.

The peak surface magnetic field is another critical parameter influencing breakdown rate. During rf pulsed operation, this field induces localized heating on the cavity surface, exceeding the material's yield strength and causing microcracks that may initiate breakdown [33]. The thermal model relating pulsed heating to peak surface magnetic field is described by the following expression [34]:

$$\Delta T = \frac{1}{\sqrt{\pi \rho}} \int_0^t \frac{R_s H^2}{\sqrt{ck(t-t')}} dt', \tag{2}$$

where ΔT is the temperature rise induced by pulsed heating. For copper cavities at room temperature, ΔT must not exceed 40 K, as determined by copper's yield strength [35]. The corresponding thermal stress induced by this temperature rise is expressed as follows:

$$\sigma = E \times \alpha \times \Delta T. \tag{3}$$

Under cryogenic conditions, copper exhibits improved electrical and mechanical properties [36,37], reducing the

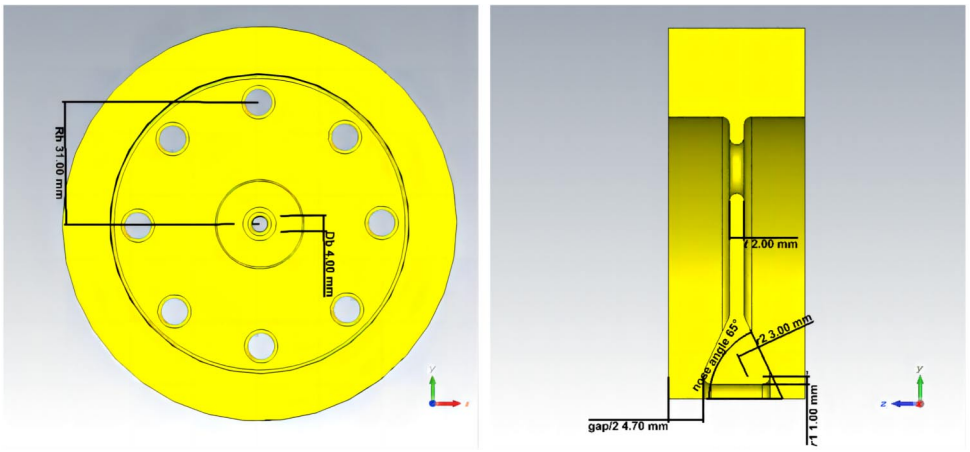


FIG. 4. Optimized cell parameters.

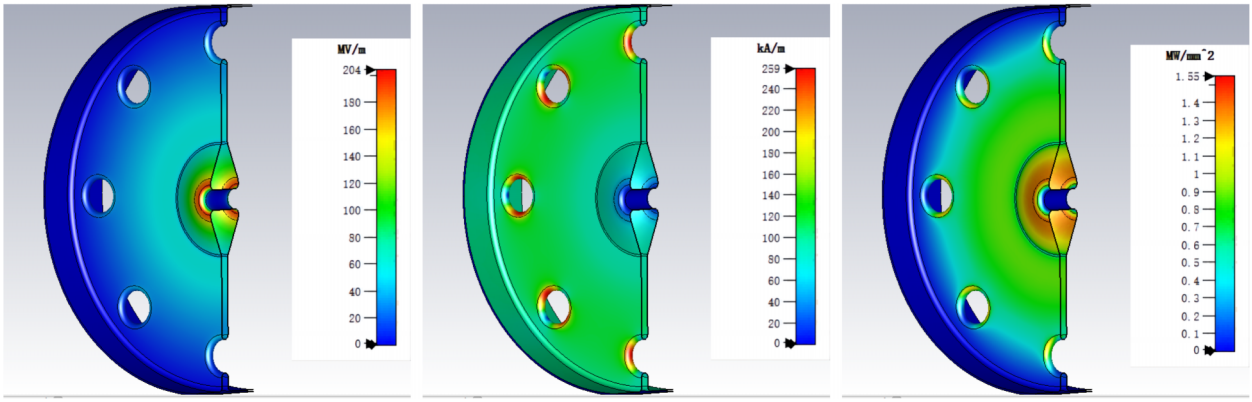


FIG. 5. Electric field (left), magnetic field (center), and modified Poynting vector (right) distributions in optimized NHS cell.

breakdown rate (BDR) induced by pulsed heating. To account for electromagnetic power influence on the maximum sustainable surface gradient, the concept of available heating power is adopted in high-gradient accelerator design. Consequently, a modified Poynting vector (S_c) is introduced [29] and defined as

$$S_c = \mathrm{Re}(S) + g_c \mathrm{Im}(S), \tag{4}$$

where S is the classical Poynting vector and $g_c = 1/6$ is an empirical constant for S-band accelerators. The scaling law relating the modified Poynting vector to the BDR is given by [38]:

$$\frac{S_c^{15} t_p^5}{\mathrm{BDR}} = \text{const.} \tag{5}$$

For a pulse length of 2500 ns and breakdown rate of 10^{-6} bpp/m under normal conductivity conditions, S_c is limited to approximately 1.75 MW/mm^2 [13]. Based on a comparative analysis of copper's physical properties at room temperature and at 77 K [36], S_c at cryogenic temperature can be increased by a factor of approximately 2.4.

B. Single cell optimization

The cell geometry was optimized to meet the constraints above. Due to its negative-harmonic design, the NHS structure has a cell length longer than that of the BTW design [7], defined as

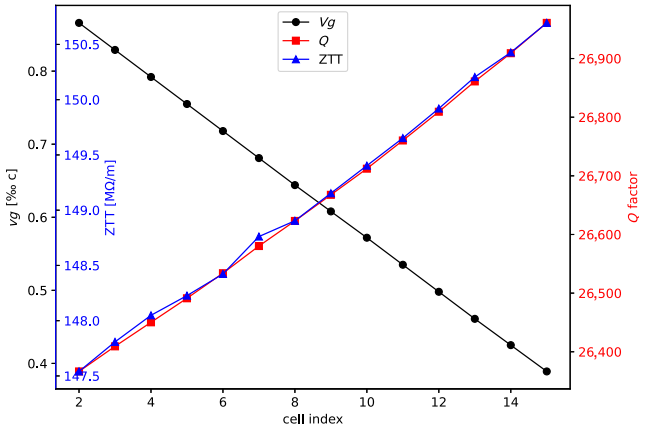


FIG. 6. Group velocity (black), Q factor (red), and ZTT (blue) distribution along the accelerating structure.

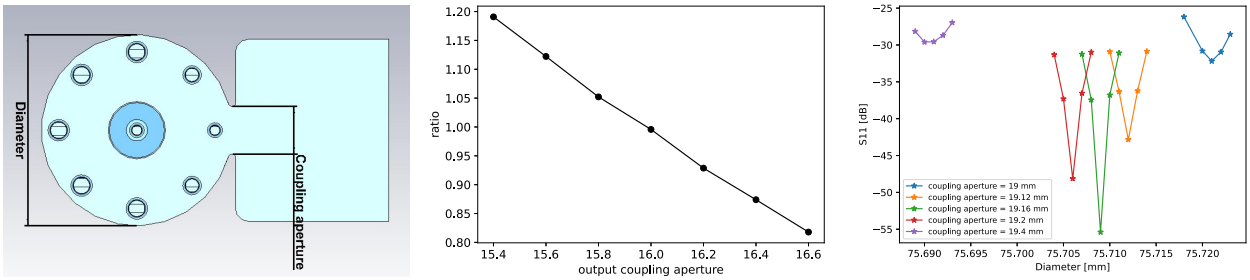


FIG. 7. Schematic of the coupler cell (left), output coupler matching response (center), and input coupler reflection coefficient (right).

$$L = \frac{\beta\lambda(\theta - 2\pi)}{2\pi}, \tag{6}$$

where β is the particle velocity normalized to the speed of light $(\frac{v}{c})$, λ is the rf wavelength, and θ is the operating mode phase advance per cell. The optimization maximizes the cell's shunt impedance while constraining the peak surface electric field to 210 MV/m, ensuring an operational safety margin for future gradient scaling. The operating mode selection is also critical, with key electromagnetic parameters summarized in Fig. 3.

As the phase advance per cell increases toward π, shunt impedance rises while group velocity decreases, resulting in increased filling time. The $5/6\pi$ mode was selected as the optimal compromise for cavity design.

The cell incorporates eight magnetically coupled ports for power transfer and a nose cone to enhance shunt impedance. The iris thickness (t) is determined by mechanical strength requirements; a 2 mm iris provides sufficient structural stability [13]. Geometric optimization focused on adjusting the nose cone profile. The final optimized cell dimensions are shown in the cross-sectional view in Fig. 4, with corresponding electromagnetic field distributions in Fig. 5.

C. Cell chain design

In traveling-wave structures, rf power is absorbed by cavity walls during transmission, causing progressive power attenuation along the structure. To maintain a constant accelerating gradient, the group velocity (Vg) must decrease linearly with length. For this magnetically coupled design, Vg is primarily adjusted by varying coupling hole dimensions at disk edges: smaller holes yield lower Vg. Concurrently, the cell radius is fine-tuned to maintain the resonant frequency at the design value. The final design achieves a group velocity range of 0.9‰c to 0.38‰c, with corresponding physical parameters listed in Fig. 6.

The Q and ZTT values of the cavity at 77 K demonstrate an approximately threefold enhancement relative to the room-temperature NHS improved design [39]. This improvement is primarily attributed to the threefold increase in the surface resistance of copper at 2856 MHz across the temperature range spanning from 77 to 300 K.

D. Coupler design

The complete structure comprises an input-cell coupler, an output-cell coupler, and 13 regular cells. Due to electromagnetic coupling between cells, the tuning process is divided into three stages: output-cell coupling adjustment, input-cell coupling adjustment, and regular cell tuning.

Matching results for both couplers are shown in Fig. 7. Output-cell coupling critically affects axial electric field uniformity. The amplitude ratio of the electric field between the output coupler and its adjacent cell was calculated for various aperture sizes to achieve a flat field profile under matched conditions. For the input coupler, aperture size and diameter were varied to ensure efficient power coupling into the cavity while maintaining the input reflection coefficient below −30 dB.

Local reflections between regular cells also need to be managed, as excessive reflections distort the axial electric field distribution. Minimizing these reflections is thus essential. The local reflection coefficient and phase advance of each cell can be derived from the simulated electric field distribution along the structure. This relationship is

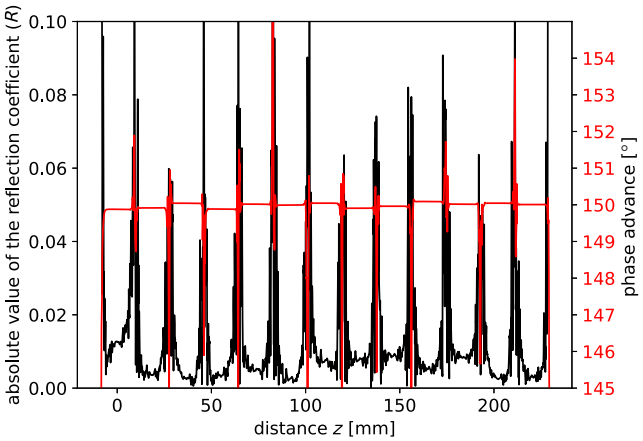


FIG. 8. Reflection coefficient and phase advance variations in regular cells (coupler cells excluded).

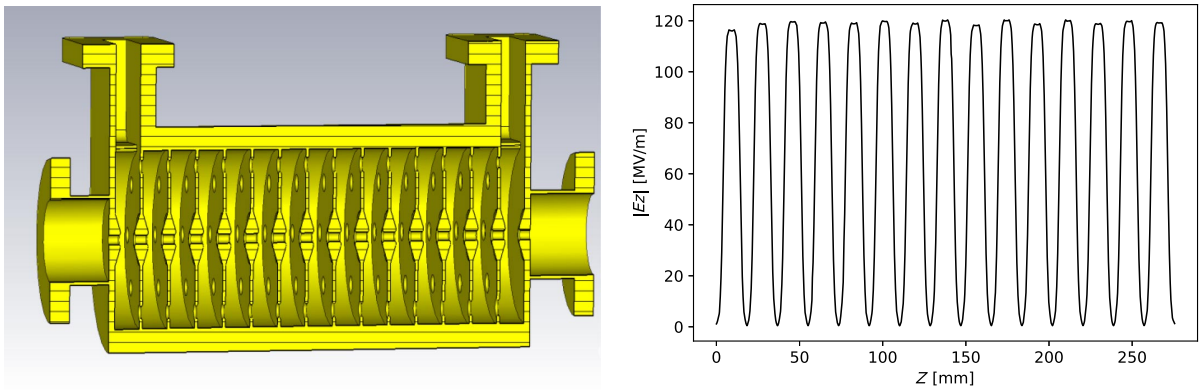


FIG. 9. Left: cross-sectional view; right: axial electric field at 77 K.

given by [40]:

$$2\cos(\psi) = \frac{E(z+D)}{E(z)} + \frac{E(z-D)}{E(z)}, \tag{7a}$$

$$\Delta(z) = \frac{E(z+D)}{E(z)} - \frac{E(z-D)}{E(z)}, \tag{7b}$$

$$R = \frac{2\sin(\varphi) - j\Delta(z)}{2\sin(\varphi) + j\Delta(z)} e^{\varphi(z)}, \tag{7c}$$

where R is the local reflection coefficient and ψ represents the phase advance. After iterative simulation-based tuning, the final per-cell reflection coefficients and phase advance obtained via Kroll's method are shown in Fig. 8. The figure displays results for 13 regular cells; the input and output coupling cells are excluded because their external electric fields vanish, rendering the method inapplicable. Uniform values correspond to the accelerating-gap region, while significant peaks arise at the nose cone tip, where greater field variation increases uncertainty in the extracted coefficients.

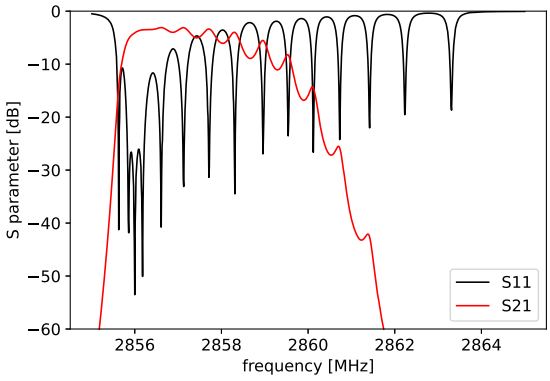


FIG. 10. S11 (black) and S21 (red) of the cryogenic NHS structure at 77 K.

E. Full cavity design

Through iterative parameter adjustments, the regular cell reflection coefficient was minimized to below 0.1 for all regular cells, while maintaining a uniform axial electric field in the cryogenic structure. The input coupler was tuned to achieve a reflection coefficient S11 below −50 dB. The resulting electric field distribution and S-parameters are shown in Figs. 9 and 10, with cavity parameters summarized in Table I.

F. Cryogenic cavity tuning studies

The rf design operates at 77 K. However, since the cavity is fabricated at room temperature, thermal scaling must account for copper contraction during cooling. As temperature decreases, the thermal expansion coefficient of copper increases [36]. The cumulative effect of this coefficient from 77 K to room temperature provides the scaling factor for cavity dimensions at fabrication temperature. This calculation shows a frequency shift of +9 MHz (upward) when cooling from 300 to 77 K, as shown in Fig. 11.

TABLE I. Physical parameters of the NHS cavity at 77 K.

Physical parameters	
Operating frequency	2856 MHz
Particle velocity, β	0.3
Operating mode	$5/6\pi$
Cavity length	275 mm
E_a	60 MV/m
Filling time	1418 ns
Working temperature	77 K
Input power	8.2 MW
Vg	0.38‰c − 0.9‰c
ZTT	147.38–150.69 MΩ/m
Q factor	26328–26969
E_{pk}	204 MV/m
H_{pk}	259 kA/m
S_c	1.55 MW/mm^2

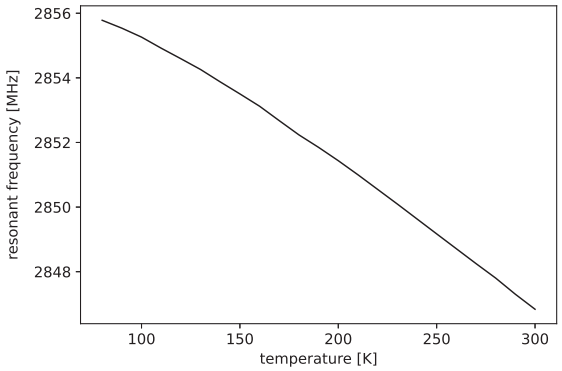


FIG. 11. Resonance frequency of an NHS cavity cell as a function of temperature.

Cavity parameters at 300 K were scaled from the cryogenic design. Simulated S11 and axial electric field distributions at 300 K are shown in Fig. 12. The scaled model exhibits S11 ≈ -20 dB at 2847 MHz, with a decreasing axial electric field profile along the structure. Most cryogenic linacs employ standing-wave structures. For such cavities, apart from input coupling considerations, the electric field distribution at cryogenic temperatures generally matches that at room temperature (Fig. 13)

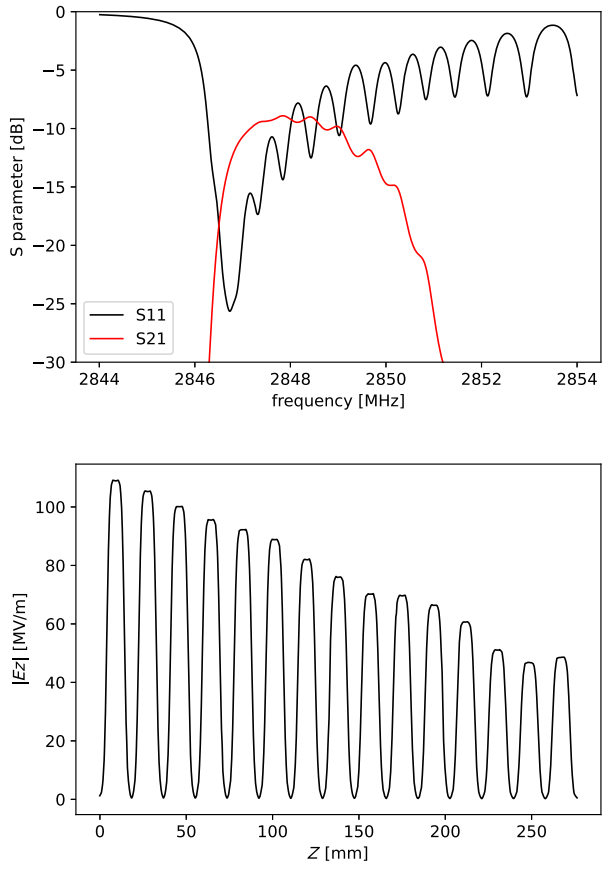


FIG. 12. Top: S-parameter of the expanded cryogenic cavity at room temperature; bottom: electric field distribution at 2847 MHz.

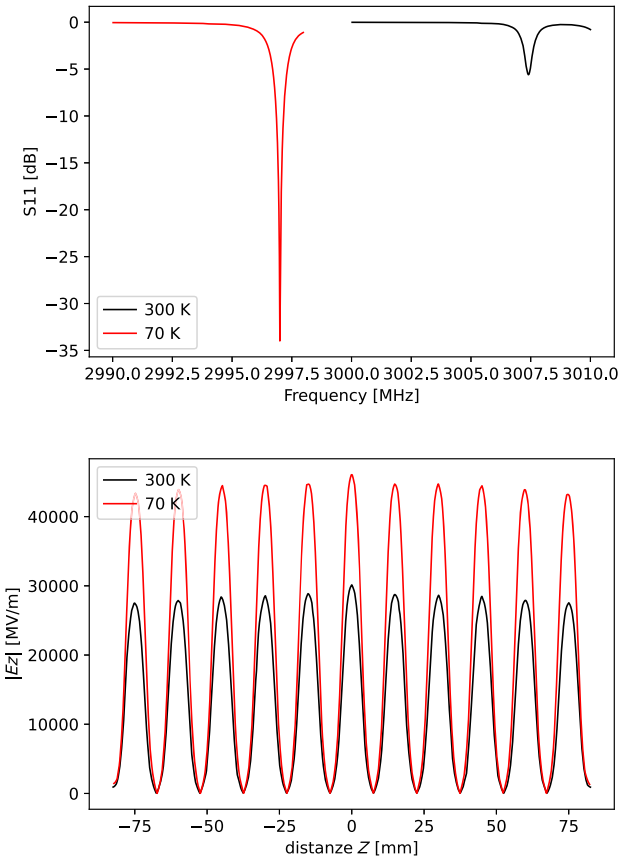


FIG. 13. S11 and axial electric field distributions of the standing-wave cavity at 300 and 77 K.

[21,41]. Consequently, tuning a cryogenic standing-wave linac can be performed at room temperature. However, electric and phase distributions in cryogenic traveling-wave cavities deviate from room-temperature values due to thermal contraction-induced shifts (from 300 to 77 K), preventing direct attainment of the target field profile via room-temperature tuning alone. To address this, we developed a specialized tuning methodology for cryogenic traveling-wave cavities. The methodology and experimental results are presented in Sec. V.

III. CONDUCTION COOLING SYSTEM DESIGN

Cryogenic modules typically employ cryocoolers or fluid cooling. The current design uses a cryocooler with a cold head thermally coupled to the cavity via copper braids, as shown in Fig. 14. The engineering design targets three subsystems: vacuum, cooling, and cavity tuning. Thermal analyses validated structural performance and feasibility using ANSYS [42]. The vacuum system comprises two distinct subsystems: the NHS cavity and the cryogenic module, each requiring different pressure thresholds. The cryogenic module must maintain a pressure below 10^{-5} mbar to suppress thermal convection [43], while the NHS cavity requires below 10^{-9} mbar to

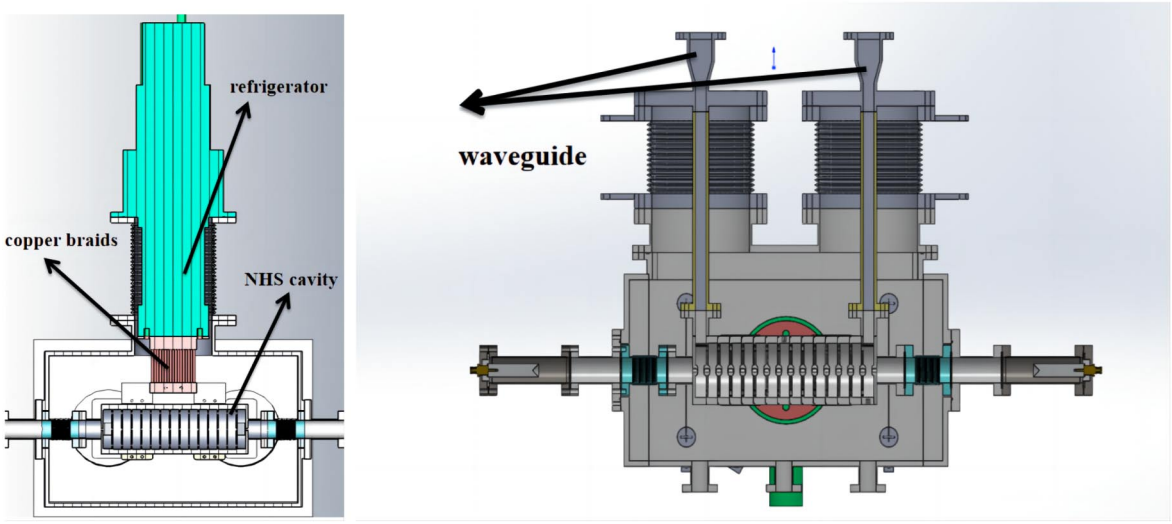


FIG. 14. Cross-sectional view of the cryogenic module design.

minimize breakdown rates. To achieve these levels, a dedicated pumping port is integrated into the cryogenic module, with evacuation ports connected to both the input and output couplers of the NHS cavity.

A. Heat leakage estimation

Heat transfer occurs via three mechanisms: conduction, convection, and radiation. In the high vacuum environment, thermal convection is negligible. Thus, only conduction and radiation between the copper cavity and module walls require consideration. To limit conductive heat loads, the cavity connects to the external environment via corrugated stainless steel braids and stainless steel waveguides—mechanically flexible components that minimize heat transfer due to stainless steel's low thermal conductivity at cryogenic temperatures.

Thermal analyses in ANSYS incorporate temperature-dependent emissivity of stainless steel (290 to 77 K) from established Ref. [44]. Specific heats and thermal conductivities of copper and stainless steel are derived from standard databases [36,45] and summarized in Table II. Simulations estimate a heat leakage of 16 W when the cavity surface stabilizes at 77 K. The temperature distribution is shown in Fig. 15. The cold head-cavity temperature difference is 10 K, with a 1.5 K gradient across the cavity. The braid-cavity interface is the coldest point, while the opposing side is the warmest.

TABLE II. Material properties of oxygen-free copper and stainless steel at 77 K.

	Oxygen-free copper	Stainless steel 304
Radiation from 290 K, surface at 77 K	0.12	0.34
Young's modulus (GPa)	132	214
Thermal conductivity [W/(mK)]	515.07	7.92
Specific heat [J/(kgK)]	198	204
Linear expansion (1/K)	7.94	−279.89

B. Multiphysics analysis for cryogenic NHS cavity

The cold head is thermally coupled to the cavity via copper braids, whose limited thermal conductivity constrains the system's power handling capacity. To dissipate rf losses, a temperature difference must be maintained between the cavity and cold head. As the total thermal load increases, this difference rises. If the thermal load exceeds the braids' conduction capacity, the cavity temperature exceeds 77 K. Thus, the cooling scheme is suitable for low repetition rate sources. Wall losses were computed in cst and imported as a heat source for thermal simulation. For a 2500 ns rf pulse at 60 MV/m, the simulated loss per pulse is 12 W.

A single-stage Gifford-McMahon (G-M) refrigerator with a nominal cooling power of 250 W at 77 K is used for preliminary experiments. Its cooling capacity versus temperature is shown in Fig. 16 [46]. The curve exhibits a linear decrease in cooling power below 77 K, incorporated into the thermal design. A conductive heat transfer boundary condition was applied at the cold head interface to model the refrigerator's temperature-dependent performance. Simulations show the cavity stabilizes at 77 K only for thermal loads below 64 W and the corresponding temperature distribution at this limit is shown in Fig. 17. This 64 W limit corresponds to a maximum repetition rate of 5 Hz for the power source.

rf power is applied once the cavity temperature stabilizes near 77 K during cooldown. This condition serves as the initial state for the steady-state thermal simulation. The resulting temperature distributions for different power-source repetition rates are shown in Fig. 18.

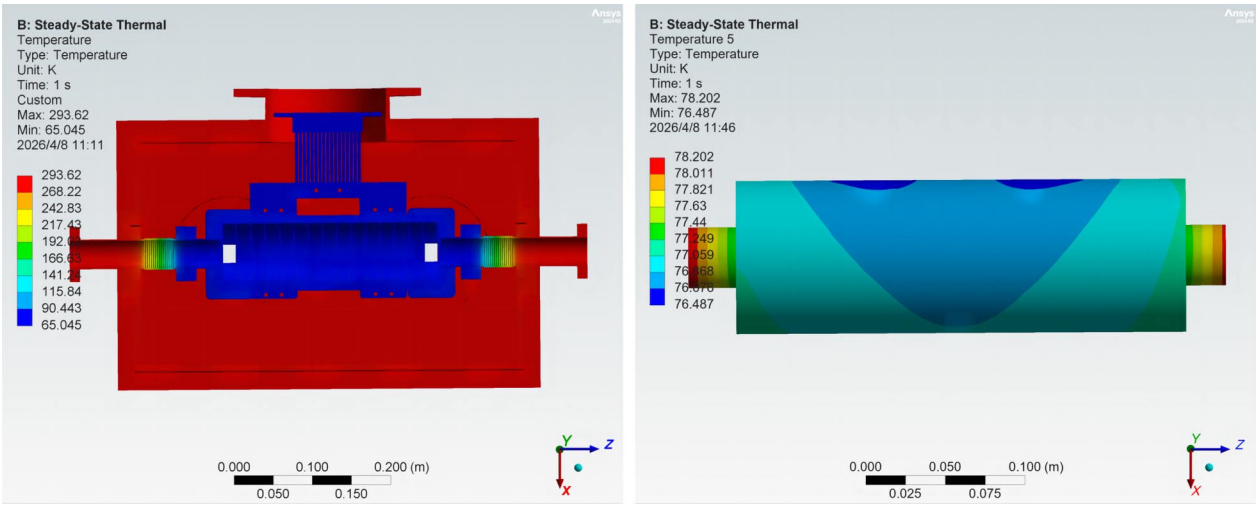


FIG. 15. Temperature distribution of cryogenic module (left) and the NHS cavity (right) with heat leakage.

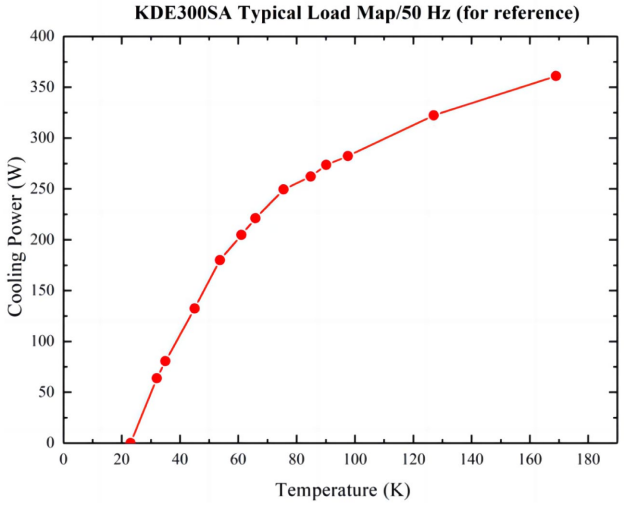


FIG. 16. Cooling capacity versus temperature for the single-stage G-M refrigerator used in this work.

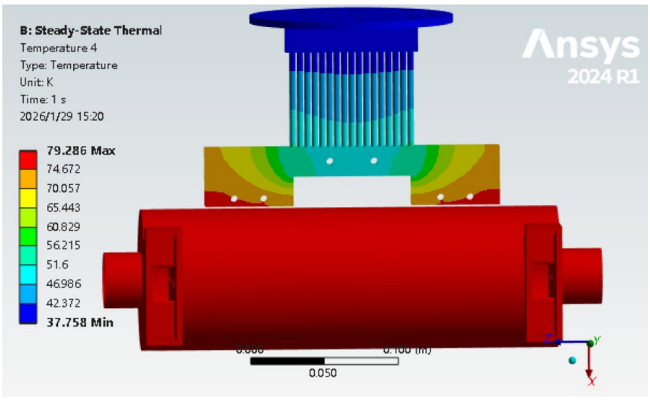


FIG. 17. Temperature distribution of the cold head and the NHS cavity under the maximum heat load of 64 W.

The cold head is connected to a single side of the cavity, maintaining a lower temperature on that side. As the repetition rate increases, the surface temperature distribution evolves accordingly. The temperature gradient across the cavity is 0.2 K/Hz. For this low heat load, the dominant gradient is observed in the transverse cross-sectional plane, while the longitudinal gradient is negligible. This nonuniform heating induces a measurable cavity axis offset, estimated as follows [47].

$$\delta = \frac{\beta_0}{D_0} \int \int \delta T dz dz, \tag{8}$$

where δ denotes the transverse offset of the cavity axis, β_0 is the linear thermal expansion coefficient, D_0 is the outer diameter of the cavity, and δT is the temperature difference between opposite sides of the cavity wall. For low repetition rate operation, δT can be treated as approximately constant and does not exceed 2 K. A temperature difference of 2 K leads to a calculated axis offset of about 0.01 mm, which is within typical machining tolerances and thus acceptable for intended operation.

Figure 19 illustrates the temperature rise induced by pulsed heating over five consecutive rf pulses. A localized temperature increase of 10 K is observed at the coupling holes near the disk edge, which is in good agreement with the theoretical prediction of 9.6 K from Eq. (2). The reduction in pulsed heating is primarily attributed to the decreased surface resistance of the copper cavity at cryogenic temperatures, coupled with the improved thermal properties at low temperatures compared to conventional room-temperature NHS designs. The observed temperature rise remains well below the cryogenic design limit of 40 K for copper structures [35].

Thermal stress generated during each rf pulse repeatedly loads the cavity wall, potentially causing fatigue damage. This stress was evaluated using a unit cell model with a

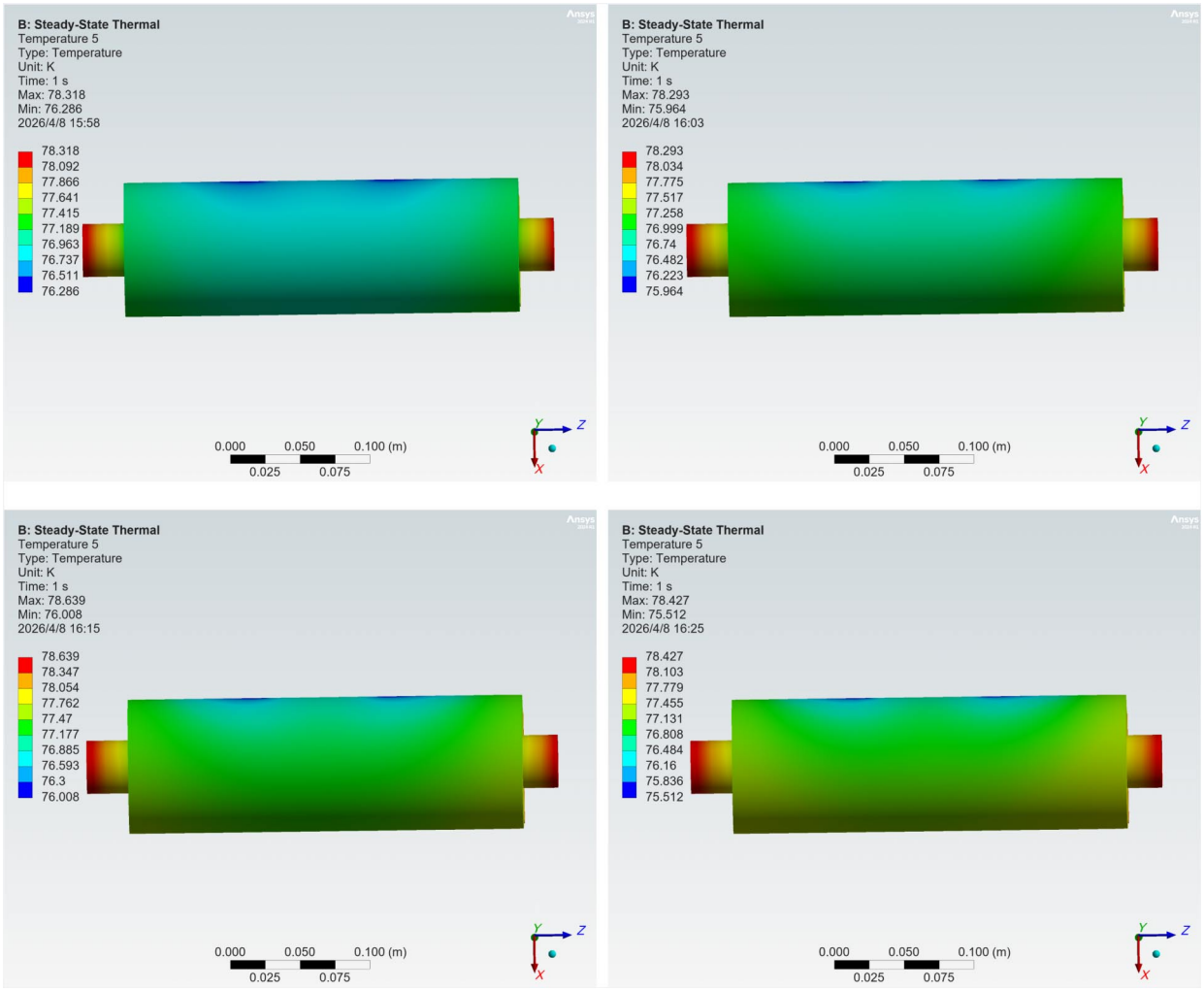


FIG. 18. Steady-state temperature distributions under rf power input at different repetition rates: 1 Hz (left, top), 2 Hz (right, top), 3 Hz (left, bottom), and 4 Hz (right, bottom).

10 K temperature rise. The von Mises stress distribution is shown in Fig. 20. The peak stress is 12 MPa, remaining well below the cryogenic yield strength of copper. Cryogenic performance metrics for the NHS cavity and module are summarized in Table III.

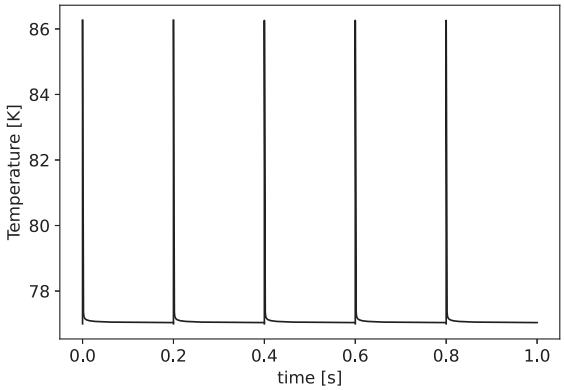


FIG. 19. Transient heating within five pulses.

C. Conduction cooling for high rf repetition rate

The aforementioned analysis is based on preliminary cavity testing and the rf repetition rate is limited to 5 Hz based on the feasibility analysis. To achieve the designed repetition rate of 120 Hz, further modifications to the cryogenic module are required. There are two aspects of improvements to the cryogenic module, replacement of higher-power refrigerator and optimization the structure of copper braids for a better transmission efficiency. Currently, the cooling capacity of G-M refrigerators could exceed 600 W at 77 K [48,49]. In this case, where the heat conduction efficiency of the copper braids is sufficiently high, the cooling capacity can be completely transferred to the cavity. At this time, three refrigerators can be added for a repetition frequency of 120 Hz.

In addition to conductive cooling, fluid cooling methods can be employed to cool cavities for higher repetition rate power sources, such as liquid nitrogen cooling. To prevent phase transition when utilizing liquid nitrogen cooling, the

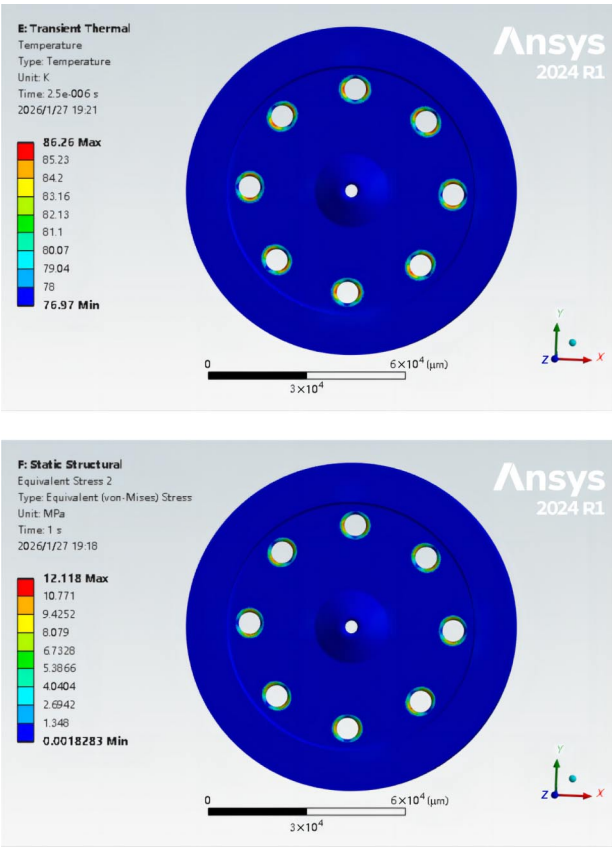


FIG. 20. Distributions after pulse heating: temperature rise (top); von Mises thermal stress (bottom).

cavity must operate at lower temperatures; an operating temperature of 70 K is adopted in this configuration. The U-shaped tubes with a diameter of 2 cm are implemented to circulate liquid nitrogen through the cavity at a flow velocity of 3 m/s. The calculated Reynolds number is $\mathrm{Re} = \rho v d/\mu \approx 2.95 \times 10^8$, which exceeds the critical value of 4000, indicating turbulent flow conditions. The Prandtl number is determined as $Pr = \mu C_p/k \approx 2.2$. Under these conditions, the system operates in the regime of turbulent forced convective heat transfer. The Dittus-Boelter correlation is commonly employed for such

TABLE III. Cryogenic performance of the NHS cavity and cryogenic module.

Parameter	Value
Accelerating gradient	60 MV/m
Pulse length	2500 ns
Heat leakage	16 W
Cooling capacity	250 W @ 77 K
Power load	60 W @ 5 Hz
Wall-plug-power for rf system	600 W
Wall-plug-power for cooling system	7.5 kW [46]
Pulse heating	10 K
Temperature gradient	2 K

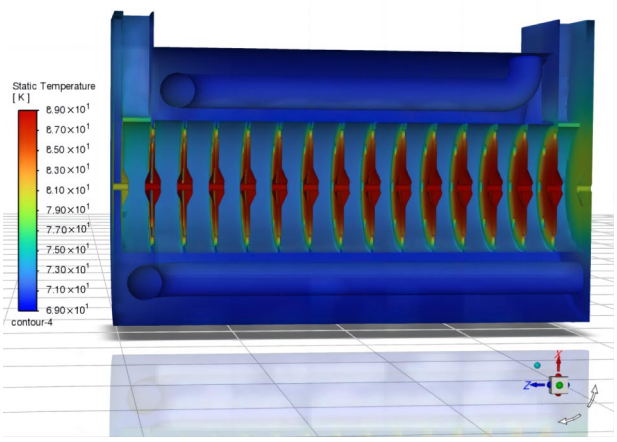


FIG. 21. Temperature distribution on cavity under liquid nitrogen cooling conduction.

scenarios, yielding the following Nusselt number (Nu) and heat transfer coefficient (h):

$$Nu = 0.023 Re^{0.8} Pr^{0.3} \approx 512, \tag{9a}$$

$$h = Nuk/d \approx 3840\ \mathrm{W/(m^2\ K)}. \tag{9b}$$

Based on the cavity length, four identical U-shaped tubes are sufficient to dissipate the heat generated by the cavity while maintaining the liquid nitrogen temperature rise below 3 K. The computational results obtained from ANSYS FLUENT are presented in Fig. 21, demonstrating that the liquid nitrogen temperature increase can be maintained within 2 K, whereas the maximum temperature rise on the cavity surface reaches 20 K.

IV. CELL FABRICATION AND TEST

Due to machining and cryogenic performance uncertainties, the cell prototype was fabricated and tested before full cavity manufacturing. The test cell is shown in Fig. 22.

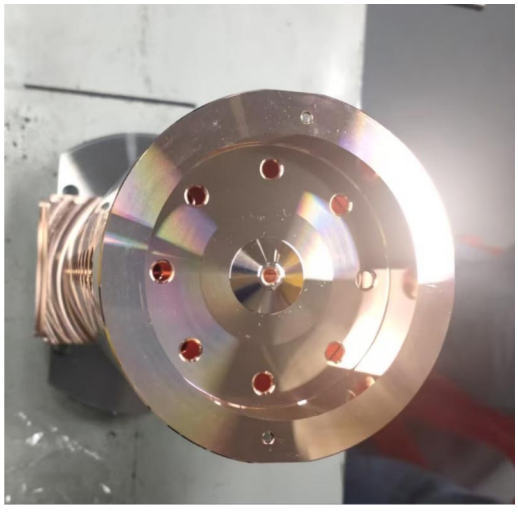


FIG. 22. Shape of fabricated NHS cell.

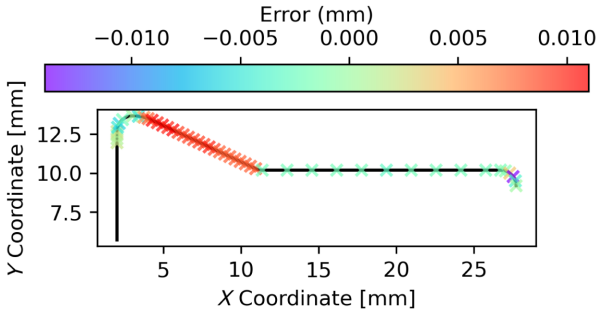


FIG. 23. Machining tolerances in nose cone geometry.

Dimensional scans of the disk contour (Fig. 23) confirm machining tolerances are within 10 μm. According to the sensitivity analysis for the optimized cell geometry (Table IV), these tolerances induce a maximum resonant frequency shift of 2.3 MHz. To verify tuning capability, a two-cell test model with six tuning holes was employed. The experimental setup is shown in Fig. 24.

A. Test method

Standing wave module made of N cells will excite $N+1$ resonant modes [50], and these modes can be expressed as

$$\phi = \frac{n\pi}{N}. \tag{10}$$

In the test model, three resonant modes are excited: π, $\pi/2$, and 0 mode. As shown in Fig. 3, the electromagnetic parameters of the π mode are close to those of the $5\pi/6$ mode. Thus, the properties of the operating mode can be accurately estimated from π mode measurements.

B. Results for the cell manufacturing test

The manufacturing procedure requires accounting for machining tolerances and dimensional changes induced by brazing. The resonant frequency and Q factor of the test cavity were simulated using cst under both atmospheric and vacuum conditions, then compared with measurements from prebrazing and postbrazing tests. In both simulation and experiment, the pickup probe was retracted to maintain weak coupling, ensuring the Q factor and resonant frequency derived from S21 closely approximate unloaded cavity characteristics. The vacuum to atmospheric frequency shift [51] follows this relationship:

$$f_v = f_m[1 + 1.7 \times 10^{-5}(T_m - T_c)]\sqrt{\varepsilon}, \tag{11a}$$

$$\varepsilon = 1 + \frac{P_a}{T_m} \times \left[211 + \frac{P_0 H_m}{P_a}\left(\frac{10160}{T_c} - 0.294\right)\right] \times 10^{-6}, \tag{11b}$$

$$P_0 = 10^{7.45 \times \frac{T_c - 273}{T_c - 38.3} + 0.656}. \tag{11c}$$

During the measurements, the ambient temperature T_m was 25 °C, the atmospheric pressure P_a was 758.46 Torr, and the relative humidity H_m was 0.378. The simulated and measured results under these conditions are summarized in Table V and Fig. 25. The measurements indicate that the Q factor of the cavity after brazing is approximately 87% of its prebrazing value due to the brazing process. In contrast, the resonant frequency of the π mode shifted by approximately 4 MHz as a result of brazing.

TABLE IV. Sensitivity analysis for optimized cell geometry.

	Sensitivity (MHz/mm)
Cell diameter D_0	−34.13
Cell length L	−33.46
Coupling hole orbit radius R_h	−0.1
Beam aperture diameter D_b	−10
Disc thickness t	30
Nose cone angle α	2.67

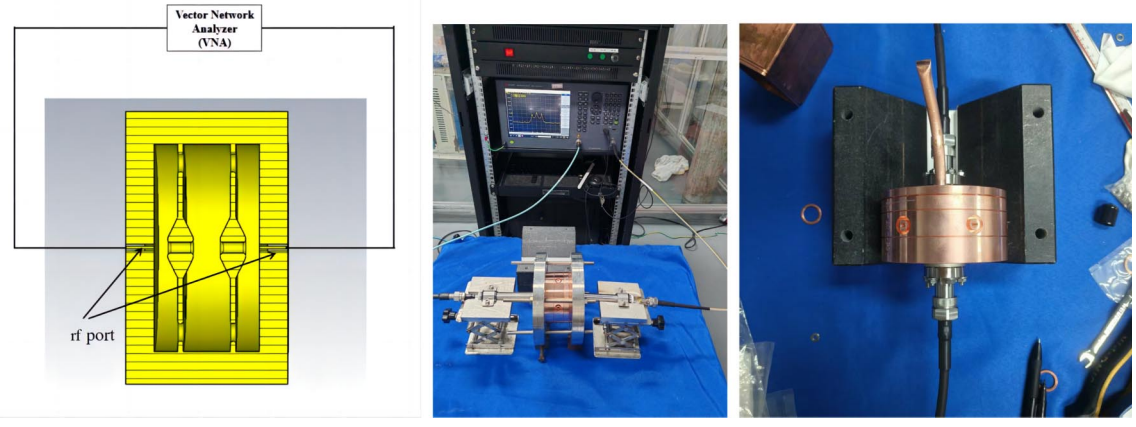


FIG. 24. Schematic diagram (left), compact splicing setup (middle), and brazing cavity (right) in cell testing.

TABLE V. Simulated and measured results for the test cavity at room temperature.

	Simulated in air	Simulated in vacuum	Measured in air before brazing	Measured in air after brazing	Measured in vacuum after brazing
The frequency of π mode (MHz)	2844.90	2845.63	2844.50	2840.87	2841.76
Q factor of π mode	6252	6323	6263	5509	5465

C. Test cell tuning studies

Tuning is critical to compensate for frequency shifts caused by machining and brazing tolerances. Resonant frequency is adjusted via mechanical deformation of dimple tuners (Fig. 26) per cell, actuated by pushing or pulling protrusions. Previous validation of this magnetic coupling cell design achieved a maximum tuning range of 6 MHz using four dimple tuners [13]. However, this configuration cannot accommodate worst case scenarios with large frequency deviations. To address this, six dimple tuners are now incorporated per cell, expanding the tuning range and ensuring robustness against frequency shifts induced by manufacturing.

In the two-cell test model, all tuners are mounted on the central full cell, while the half cells have no tuners. The measured frequency shift of the two-cell model was converted to equivalent single cell tuning sensitivity.

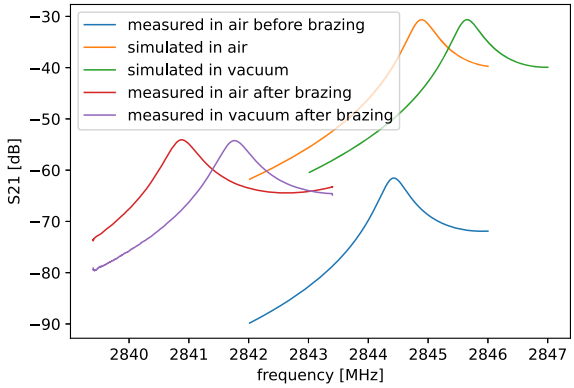


FIG. 25. Simulated and measured power transmission S21 for the test.

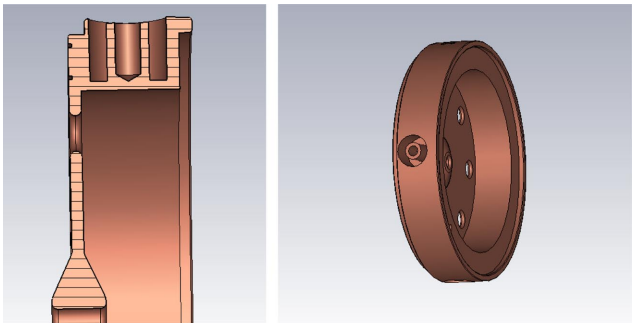


FIG. 26. Machining drawings of the dimples and cell tuning holes.

Simulated and experimental tuning curves are shown in Fig. 27. These results demonstrate an 8 MHz tuning range for 2 mm tuner displacement per cell.

Destructive tests determined the mechanical limits of the tuning system. The maximum achievable tuner displacement is 4 mm, beyond which further deformation is limited by increasing stress. A cross-sectional view of the cavity after destructive testing is shown in Fig. 28. The available tuning range fully covers expected manufacturing-induced

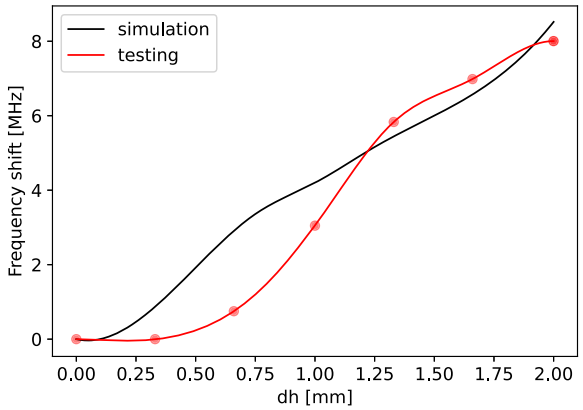


FIG. 27. Tuning capability comparison for the six dimple tuners: simulation (black) versus experimental measurement (red).

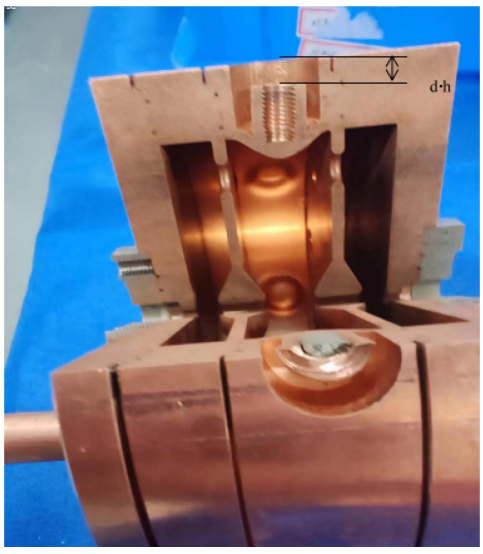


FIG. 28. Cross section of the test cavity after completion of tuning and destructive test.

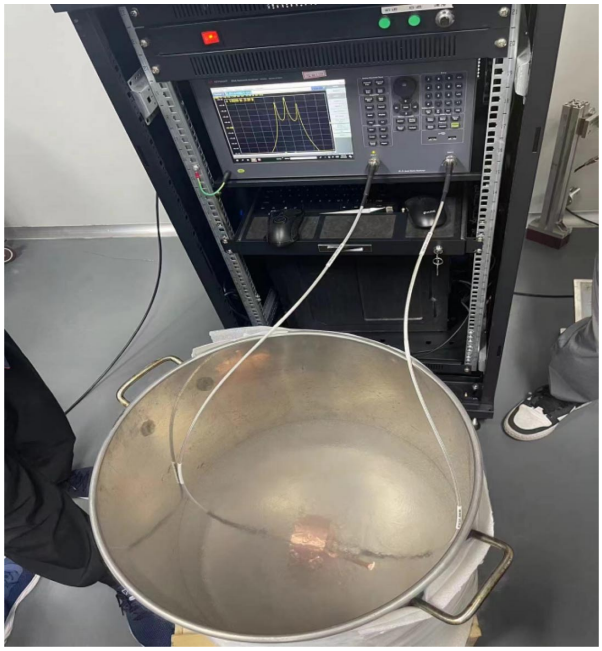


FIG. 29. Experimental setup for the cell test in liquid nitrogen.

TABLE VI. Resonant frequency and Q factor of the test cavity at room temperature (300 K) and in liquid nitrogen (77 K).

	Room temperature	Liquid nitrogen
Frequency (MHz)	2841.76	2851.61
Q factor	5465	15957

frequency errors, confirming the design can be adequately tuned postfabrication.

D. Cryogenic characteristics

The frequency shift and Q factor variation between room temperature and cryogenic operation are critical performance metrics. To evaluate these, the test cavity was immersed in liquid nitrogen (77 K), and its resonant frequency and Q factor were measured. The experimental setup is shown in Fig. 29, with results summarized in Table VI and plotted in Fig. 30. Experimental results demonstrate a 9.85 MHz resonant frequency shift and a 2.9-fold increase in Q factor when transitioning from room temperature to 77 K. The measured data show excellent agreement with simulation.

V. FULL CAVITY RF MEASUREMENTS AND TUNING

After cell testing, cryogenic prototype manufacturing was completed. Tuning is critical for the full cryogenic cavity due to machining tolerances and brazing-induced deformations. Direct adjustment of the traveling-wave cavity at room temperature is impractical due to field

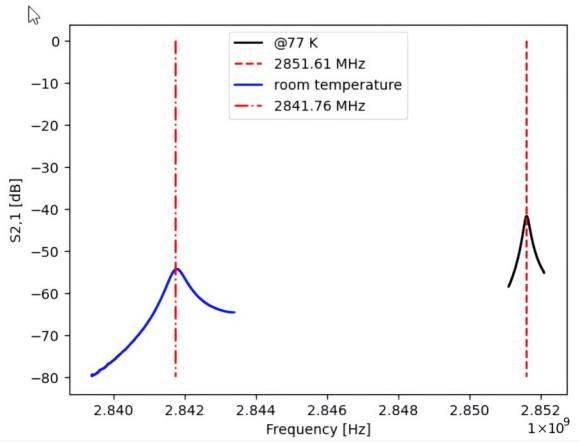


FIG. 30. Transmission coefficient S21 of the test cavity measured at room temperature (300 K) and under cryogenic conditions (77 K).

distribution changes between room-temperature and cryogenic conditions. Therefore, an optimized tuning protocol was developed, comprising the following steps: (i) Measure the axial electric field distribution under cryogenic operating conditions using the nonresonant perturbation method [52]. (ii) Analyze the individual cell detunings [40,52] based on the cryogenic field distribution and convert them into corresponding dimensional adjustments required at room temperature. (iii) Perform the physical tuning of the cavity at room temperature according to the converted dimensional targets.

The process will be repeated multiple times until the cavity meets all target specifications under cryogenic operating conditions.

A. Full cavity cryogenic testing platform design

Measuring the axial electric field distribution in a full cryogenic cavity poses a significant technical challenge, primarily because an ultrahigh vacuum must be maintained to avoid ice formation on internal surfaces. To overcome this difficulty, we have designed and built the dedicated test platform illustrated in Fig. 31. Cryogenic motors are mounted at both ends of the full cavity within vacuum chambers. A fish line connects to each motor, with the perturbation probe, a stainless steel capillary tube, threaded through the line. During electric field measurements, motor activation drives the capillary tube along the cavity axis. A disc-shaped positioning plate featuring a central hole is integrated into the vacuum chamber to maintain the probe's axial alignment.

B. Cryogenic prototype tuning

Cryogenic testing was performed in liquid nitrogen, with the experimental setup illustrated in Fig. 32. The S11 magnitude was measured as the perturbation probe traversed the cavity using a vector network analyzer.

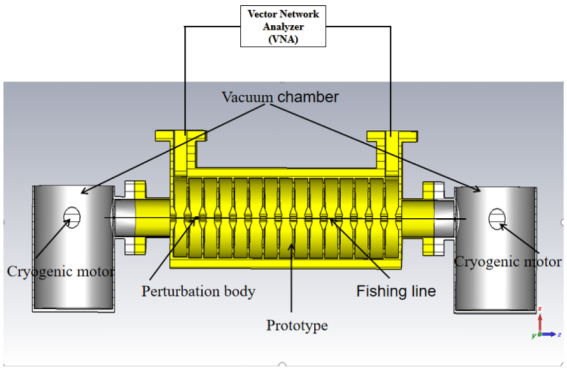


FIG. 31. Schematic of the low temperature perturbation test platform.

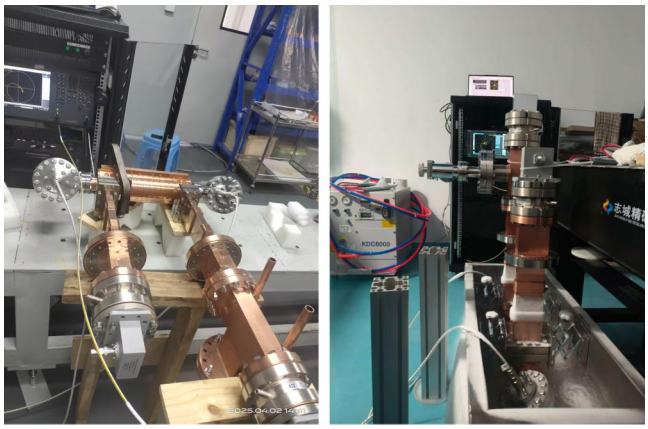


FIG. 32. Setup for room-temperature (left) and cryogenic (right) electric field distribution measurements.

The initial electric field profile within the cryogenic cavity is shown in Fig. 33. The perturbation probe with 0.02 mm outer diameter induced minimal field perturbation, demanding high-precision measurement capabilities.

Initial S11 measurements exhibited limited resolution (± 0.1), resulting in errors in local field amplitude. Despite this, a clear field distribution trend was observed, with pronounced detuning at the cavity ends. Subsequent measurements utilized improved calibration protocols to achieve ± 0.001 precision.

After two tuning iterations, the electric field profile and S11 response are shown in Fig. 34. The reflection coefficient achieved S11 below -20 dB, with a maximum cumulative phase advance deviation of 7.8°. However, the large output coupler aperture caused coupling mismatch, limiting field flatness to 84% of the theoretical maximum. Excluding the fixed output coupler aperture constraint, the tuned performance closely matched the design specifications. This confirms the effectiveness of the proposed tuning scheme for cryogenic traveling-wave cavities.

C. Conduction cooling test

Following cavity tuning completion, the cavity was integrated into the cryomodule for thermal characterization. The thermal test setup and results are shown in Figs. 35 and 36. The cavity achieved a stable temperature of 77 ± 0.3 K within 5 h of cooldown initiation from room temperature.

During cryomodule operation, the cryocooler was operated at 100% capacity, but the cavity temperature failed to stabilize at 77 K. To measure heat leakage, three heating elements were activated to maintain the cavity at 77 K. The system heat leakage, defined as the difference between the cryocooler's cooling capacity and the heating power supplied by the elements, is summarized in Table VII. According to the cryocooler head test report, the cooling capacity exhibits a maximum orientation-dependent deviation of 20%. The measured heat leakage of 35 W falls within the acceptable range of simulation results.

VI. SUMMARY AND FUTURE PLAN

In this paper, a $\beta = 0.3$, 15 cell cryogenic traveling-wave cavity was designed and fabricated. Cell optimization achieved a shunt impedance of 150 MΩ/m and a Q factor of 26,400, representing a 2.9 times improvement over room temperature performance. Based on this optimization, a cryogenic S-band high-gradient NHS cavity was developed, with a theoretical accelerating gradient limit of 60 MV/m.

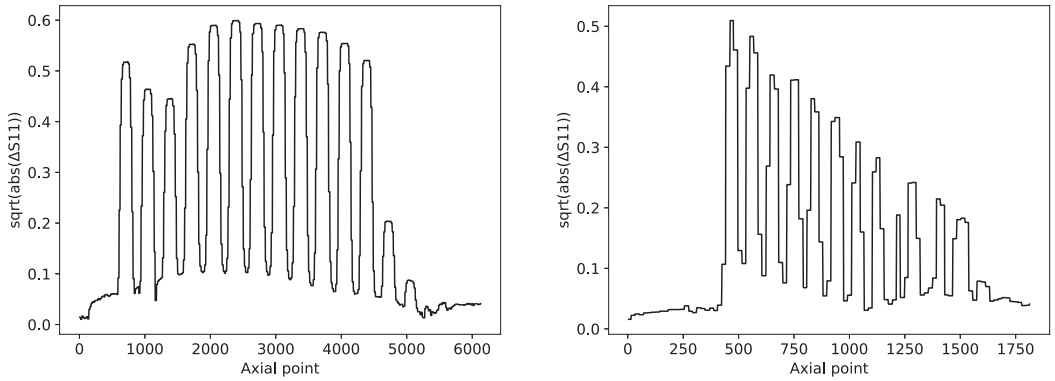


FIG. 33. Initial electric field distribution along the cavity axis at low temperature (left) and room temperature (right).

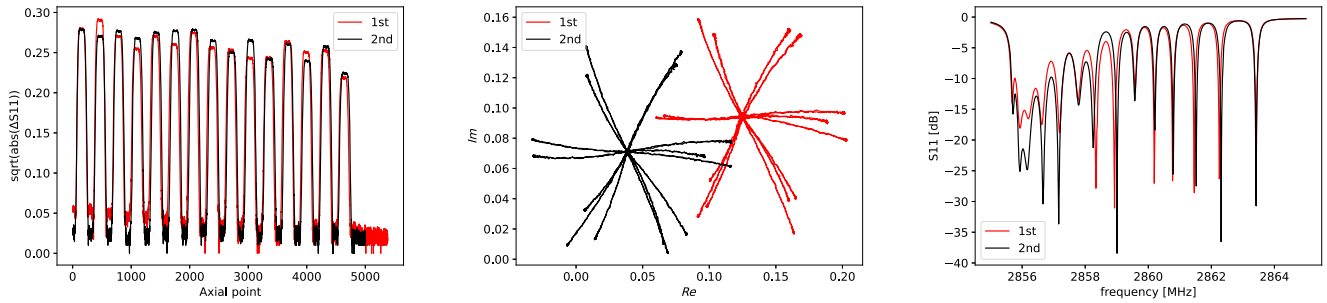


FIG. 34. First (red) and second (black) tuning iterations: on-axis electric field amplitude (left), electric field in complex plane (middle), and S11 magnitude (right).

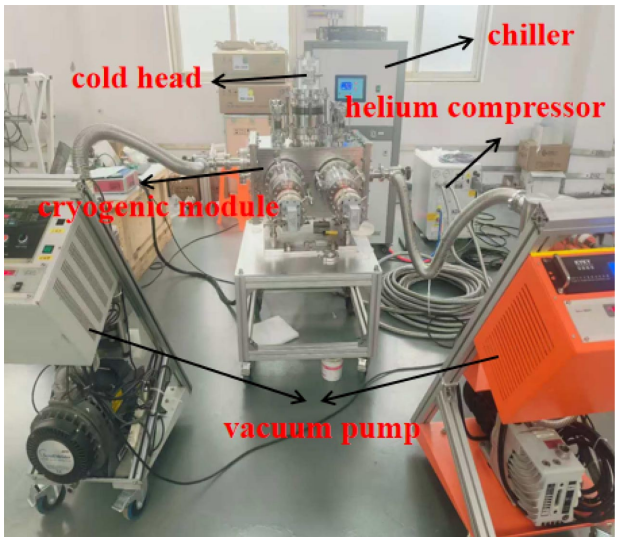


FIG. 35. Conduction cooling test diagram.

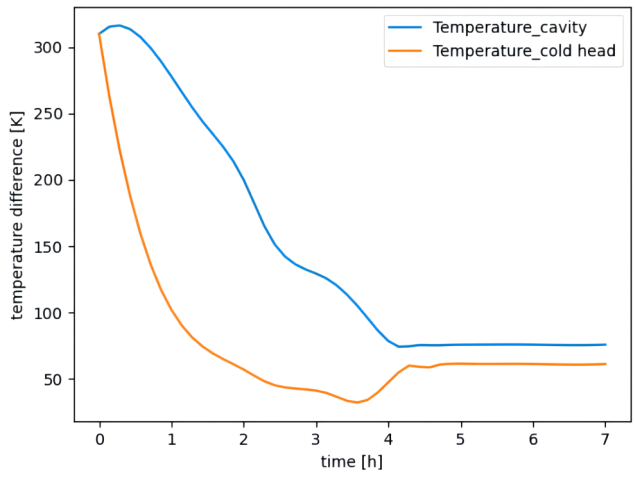


FIG. 36. Cooling curve of the conduction cooling test.

TABLE VII. Heat leakage measurement.

Cold head temperature	Cooling capacity	Power of heater 1	Power of heater 2	Power of heater 3	Heat leakage
69 K	225 W	64.71 W	61.66 W	63.81 W	34.82 W

Cell testing validated manufacturing tolerances and cryogenic performance. The results demonstrate that cavity tuning compensates for manufacturing errors, with the NHS cell exhibiting a frequency shift of 9.85 MHz from room temperature to 77 K and a quality factor increase of 2.9 times. This quantifiable relationship provides a design framework for future cryogenic traveling-wave cavities.

Following cell validation, the full cavity was fabricated and tuned. The traveling-wave design differs fundamentally from conventional cryogenic standing-wave linacs, requiring iterative tuning. The tuning methodology presented here provides a validated framework for future cryogenic traveling-wave linacs.

Future work will focus on high-power testing to verify the maximum achievable accelerating gradient of the cryogenic NHS structure, which is meaningful for the future high-gradient ultracompact linacs for hadron therapy development.

ACKNOWLEDGMENTS

This work was supported by the Gansu Provincial Major Science and Technology Project (No. 202ZJR9KA003) and National Natural Science Foundation of China (NSFC, Grant No. 12575161). The authors gratefully acknowledge the technical guidance and support from Dr. Guan Shu and Hangyevac (Shanghai) for their contributions to this research.

DATA AVAILABILITY

The data that support the findings of this article are not publicly available because they contain commercially sensitive information. The data are available from the authors upon reasonable request.

[1] W. Tinganelli and M. Durante, Carbon ion radiobiology, Cancers **12**, 3022 (2020).

[2] Particle Therapy Cooperative Group, Facilities in operation (public), https://www.ptcog.site/index.php/facilities-in-operation-public.

[3] K. Peach, P. Wilson, and B. Jones, Accelerator science in medical physics, Br. J. Radiol. **84**, S4 (2011).

[4] R. Hamm, K. Crandall, and J. Potter, Preliminary design of a dedicated proton therapy linac, in *Proceedings of the Conference Record of the 1991 IEEE Particle Accelerator Conference* (1991), Vol. 4, pp. 2583–2585, 10.1109/PAC.1991.165037.

[5] S. Benedetti, A. Grudiev, and A. Latina, High gradient linac for proton therapy, Phys. Rev. Accel. Beams **20**, 040101 (2017).

[6] U. Amaldi, S. Braccini, and P. Puggioni, High frequency linacs for hadron therapy, Rev. Accel. Sci. Techol. **02**, 111 (2009).

[7] S. V. Kutsaev, R. Agustsson, S. Boucher, R. Fischer, A. Murokh, B. Mustapha, A. Nassiri, P. N. Ostroumov, A. Plastun, E. Savin, and A. Y. Smirnov, High-gradient low-β accelerating structure using the first negative spatial harmonic of the fundamental mode, Phys. Rev. Accel. Beams **20**, 120401 (2017).

[8] S. Verdú-Andrés, U. Amaldi, and Á. Faus-Golfe, CABOTO, a high-gradient linac for hadrontherapy, J. Radiat. Res. **54**, i155 (2013).

[9] A. Degiovanni, G. De Michele, R. Bonomi, F. Magallanes, M. Caldara, V. Dimov, M. Esposito, D. Fink, M. Gallas, Y. Ivanisenko, A. Jeff, S. Magnoni, L. Quirante, H. Pavetits, A. Valloni, J. Adam, D. Murciano, S. Aumon, C. Baccigalupi, and C. Zannini, Design, integration, and commissioning of the first linac for image guided hadron therapy prototype, Phys. Rev. Accel. Beams **27**, 054701 (2024).

[10] W. Qin, Y. Huang, Y. He, W. Dou, Z. Wang, X. Jin, Z. Zhang, C. Li, R. Wang, Y. Xin, and L. Shi, S-band high-gradient low β single-periodic magnetically coupled standing-wave accelerating structure for a proton therapy linac, Phys. Rev. Accel. Beams **27**, 092002 (2024).

[11] U. Amaldi, R. Bonomi, S. Braccini, M. Crescenti, A. Degiovanni, M. Garlaschè, A. Garonna, G. Magrin, C. Mellace, P. Pearce, G. Pittà, P. Puggioni, E. Rosso, S. Verdù Andrés, R. Wegner, M. Weiss, and R. Zennaro, Accelerators for hadrontherapy: From Lawrence cyclotrons to linacs, Nucl. Instrum. Methods Phys. Res., Sect. A **620**, 563 (2010).

[12] Y. Zhang, W.-C. Fang, X.-X. Huang, J.-H. Tan, C. Wang, C.-P. Wang, and Z.-T. Zhao, Design, fabrication, and cold test of an S-band high-gradient accelerating structure for compact proton therapy facility, Nucl. Sci. Tech. **32**, 11 (2021).

[13] S. Benedetti, High-gradient and high-efficiency linear accelerators for hadron therapy, Ph.D. thesis, École Polytechnique Fédérale de Lausanne, Lausanne, Switzerland, 2018, 10.5075/epfl-thesis-8246.

[14] S. Döbert, C. Adolphsen, G. Bowden, D. Burke, and J. Chan, High gradient performance of NLC/GLC X-band accelerating structures, in *Proceedings of the 2005 Particle Accelerator Conference* (2005), pp. 372–374, 10.1109/PAC.2005.1590438.

[15] S. V. Kutsaev, R. Agustsson, S. Boucher, O. Chimalpopoca, D. Meyer, A. Murokh, B. Mustapha, A. Nassiri, A. Yu Smirnov, T. Smith, and Y. Yang, Test results of a high-gradient 2.856-GHz negative harmonic accelerating waveguide, IEEE Microw. Wirel. Componen. Lett. **31**, 1098 (2021).

[16] V. Dolgashev, S. Tantawi, C. Nantista, Y. Higashi, and T. Higo, Rf breakdown in normal conducting single-cell structures, in *Proceedings of the 2005 Particle Accelerator Conference* (2005), pp. 595–59910.1109/PAC.2005.1590501.

[17] M. Jacewicz, I. Profatilova, P. Szaniawski, I. Popov, Y. Ashkenazy, S. Calatroni, and W. Wuensch, Surface and sub-surface modifications of copper electrodes exposed to electric high-field conditioning at cryogenic temperatures, J. Appl. Phys. **137**, 193302 (2025).

[18] G. E. H. Reuter and E. H. Sondheimer, The theory of the anomalous skin effect in metals, Nature (London) **161**, 394 (1948).

[19] C. Vernieri *et al.*, A "cool" route to the Higgs boson and beyond. The cool copper collider, J. Instrum. **18**, P07053 (2023).

[20] J. B. Rosenzweig, N. Majernik, R. R. Robles, G. Andonian, and D. Cocco, An ultra-compact x-ray free-electron laser, New J. Phys. **22**, 093067 (2020).

[21] E. Nanni, Cold-copper R&D update, in *Proceedings of the 16th Workshop on Breakdown Science and High Gradient Accelerator Technology, Mérida, Yucatán, Mexico* (2025), https://indico.fnal.gov/event/65159/contributions/311816/.

[22] Q. Zhao, The low beta S-band high-gradient cryogenic copper cavity studies at IMP, in *Proceedings of the 16th Workshop on Breakdown Science and High Gradient Accelerator Technology, Mérida, Yucatán, Mexico* (2025), https://indico.fnal.gov/event/65159/contributions/311858/.

[23] P. J. Eifel, Chapter 4: A multidisciplinary approach to cancer: A radiation oncologist's view, in*Oncologic Imaging: A Multidisciplincary Approach*, 2nd ed. (W.B Saunders, Philadelphia, PA, 2023), pp. 19–27, 10.1016/B978-0-323-69538-1.00004-5.

[24] P. Nilsson, A. Gunnlaugsson, L. Beckman, A. Widmark, P. Fransson, M. Hoyer, M. Lagerlund, J. Kindblom, B. Johansson, K. Björnlinger, C. Ginman, M. Olsson, M. Agrup, E. Kjellén, B. Zackrisson, B. Tavelin, L. Franzén, H. Anderson, and C. Thellenberg Karlsson, Ultra-hypofractionated versus conventionally fractionated radiotherapy for localised prostate cancer (HYPO-RT-PC): 10-year outcomes of an open-label, randomised, phase 3, non-inferiority trial, Lancet Oncol. **27**, 293 (2026).

[25] F. Sourial, C. Champ, and S. Beriwal, The critical role of dose homogeneity in modern breast hypofractionation, Int. J. Radiat. Oncol. Biol. Phys. (2026).

[26] R. Schulte, C. Johnstone, S. Boucher, E. Esarey, C. G. R. Geddes, M. Kravchenko, S. Kutsaev, B. W. Loo, F. Méot, B. Mustapha, K. Nakamura, E. A. Nanni, L. Obst-Huebl, S. E. Sampayan, C. B. Schroeder, K. Sheng, A. M. Snijders, E. Snively, S. G. Tantawi, and J. Van Tilborg,

Transformative technology for FLASH radiation therapy, Appl. Sci. **13**, 5021 (2023).
[27] Dassault Systèmes, CST Studio Suite (2019), https://www.3ds.com/.
[28] J. W. Wang and G. A. Loew, Field emission and rf breakdown in high-gradient room-temperature linac structured, in *Frontiers of Accelerator Technology* (1999), pp. 768–794, 10.1142/9789814447324_0024.
[29] A. Grudiev, S. Calatroni, and W. Wuensch, New local field quantity describing the high gradient limit of accelerating structures, Phys. Rev. ST Accel. Beams **12**, 102001 (2009).
[30] M. Nasr, E. Nanni, M. Breidenbach, S. Weathersby, M. Oriunno, and S. Tantawi, Experimental demonstration of particle acceleration with normal conducting accelerating structure at cryogenic temperature, Phys. Rev. Accel. Beams **24**, 093201 (2021).
[31] A. Degiovanni, High gradient proton linacs for medical applications, Ph.D. thesis, École Polytechnique Fédérale de Lausanne (EPFL), Lausanne, Switzerland, 2014, 10.5075/epfl-thesis-6069.
[32] A. Cahill, G. Bowden, V. Dolgashev, A. Fukasawa, J. Rosenzweig, and S. Tantawi, High gradient S-band cryogenic accelerating structure for rf breakdown studies, in *Proceedings of the 2nd North American Particle Accelerator Conference* (2017), WEPOB42, 10.18429/JACoW-NAPAC2016-WEPOB42.
[33] D. Pritzkau and R. H. Siemann, Results of an RF pulsed heating experiment at SLAC, Stanford linear accelerator center, 2000, 10.2172/763845.
[34] D. P. Pritzkau and R. H. Siemann, Experimental study of rf pulsed heating on oxygen free electronic copper, Phys. Rev. ST Accel. Beams **5**, 112002 (2002).
[35] H. M. Musal, Thermomechanical stress degradation of metal mirror surfaces under pulsed laser irradiation, ASTM Special Technical Publications (1980), p. 159, https://api.semanticscholar.org/CorpusID:134530710.
[36] N. Simon, E. Drexler, and R. Reed, Properties of copper and copper alloys at cryogenic temperatures, National Institute of Standards and Technology, Gaithersburg, MD, 1992, 10.6028/NIST.MONO.177.
[37] J. Srnec Novak, D. Benasciutti, F. De Bona, A. Stanojević, and P. Huter, Thermo-mechanical finite element simulation and fatigue life assessment of a copper mould for continuous casting of steel, Proc. Eng. **133**, 688 (2015).
[38] S. Verdú Andrés, High-gradient accelerating structure studies and their application in hadrontherapy, Ph.D. thesis, Universitat de València, Burjassot-Paterna, Spain, 2013, http://hdl.handle.net/10261/90425.
[39] S. Kutsaev, R. Agustsson, A. C. Araujo Martinez, V. Dolgashev, B. Mustapha, A. Smirnov, S. Thielk, and G. Ye, High-gradient accelerating structure for hadron therapy linac, operating at kHz repetition rates, in *Proceedings of the Linear International Accelerator Conference (LINAC2022)* (JACoW, Geneva, Switzerland, 2022), MOPOPA22, 10.18429/JACoW-LINAC2022-MOPOPA22.
[40] N. M. Kroll, C. K. Ng, and D. C. Vier, Applications of time domain simulation to coupler design for periodic structures, arXiv:physics/0008201.
[41] Z. Gao, The development of C-band cryogenic high-gradient structures for SXFEL, in *Proceedings of the 16th Workshop on Breakdown Science and High Gradient Accelerator Technology, Mérida, Yucatán, Mexico* (2025), https://indico.fnal.gov/event/65159/contributions/311856/.
[42] ANSYS, Inc., ANSYS 2024 R1 (2024), https://www.ansys.com/products.
[43] P. Cruikshank, G. Engelmann, W. Koelemeijer, N. Kos, and A. G. Mathewson, Insulation vacuum system of the LHC, Vacuum **48**, 759 (1997).
[44] P. Lebrun, An introduction to cryogenics, Technical Report, CERN, Geneva, 2007, 10.17181/CERN.KOEP.SD6C.
[45] NIST, Material properties: 304 stainless (UNS s30400), https://trc.nist.gov/cryogenics/materials/304Stainless/304Stainless_rev.htm.
[46] CSIC cryopride product descriptions, https://www.cryosrv.com/wp-content/uploads/2024/11/KDE300SA.pdf.
[47] G. Wang, Temperature distribution within the electron linear accelerator and its impact on the accelerator's performance, J. Nanjing Univ. Technol. **1**, 19 (1979) [in Chinese].
[48] AL600 with CPA1114 cryocooler capacity curve, https://cdn.bluefors.com/wp-content/uploads/2024/10/30085605/AL600-CPA1114-Cryocooler-Capacity-Curve.pdf.
[49] CH-160D3 77 K cryocooler series, https://shicryogenics.com/product/ch-160d3-77k-cryocooler-series/.
[50] S.-Y. Lee, *Accelerator Physics*, 4th ed. (World Scientific, Singapore,2018), 10.1142/11111.
[51] T. Khabiboulline, V. Puntus, R. Dohlus, N. Holtkamp, G. Kreps, S. Ivanov, and K. Jin, A new tuning method for traveling wave structures. *Proceedings Particle Accelerator Conference* (IEEE, New York, 1995), Vol. 3, pp. 1666–1668, 10.1109/PAC.1995.505321.
[52] W. Fang, Q. Gu, Z. Zhao, and D. Tong, The nonresonant perturbation theory based field measurement and tuning of a linac accelerating structure, Sci. China Phys. Mech. Astronomy **56**, 2104 (2013).